Improved Modeling and Understanding of Diffusion-Media Wettability on Polymer-Electrolyte-Fuel-Cell Performance

Adam Z. Weber

Environmental Energy Technologies Division
Lawrence Berkeley National Laboratory
1 Cyclotron Rd, MS 70-108B, Berkeley, California 94720, USA

A macroscopic-modeling methodology to account for the chemical and structural properties of fuel-cell diffusion media is developed. A previous model is updated to include for the first time the use of experimentally measured capillary pressure – saturation relationships through the introduction of a Gaussian contact-angle distribution into the property equations. The updated model is used to simulate various limiting-case scenarios of water and gas transport in fuel-cell diffusion media. Analysis of these results demonstrate that interfacial conditions are more important than bulk transport in these layers, where the associated mass-transfer resistance is the result of higher capillary pressures at the boundaries and the steepness of the capillary pressure – saturation relationship. The model is also used to examine the impact of a microporous layer, showing that it dominates the response of the overall diffusion medium. In addition, its primary mass-transfer-related effect is suggested to be limiting the water-injection sites into the more porous gas-diffusion layer.

Electrochemical Society Active Member
E-mail: azweber@lbl.gov

Introduction

Polymer-electrolyte fuel cells (PEFCs) show great promise in becoming energy-delivery devices for a variety of future technologies. It is well known that water management is a critical component for successful PEFC operation, especially under conditions where liquid water is present (*e.g.*, low temperature, startup and shutdown, *etc.*). It is also critical for good PEFC durability and lifetime. A key component of the cell's water management is the diffusion medium (DM), often comprised of the macroporous gas-diffusion layer (GDL) and a microporous layer (MPL). To understand multiphase flow through the DM and transport throughout the PEFC, mathematical modeling has been utilized due to the complex nature of the materials and phenomena. Recently, several reviews have been published exploring the various models for DM and PEFC water management [1-4].

The modeling approaches extend across many length scales and complexities (e.g., from microscopic lattice-Boltzmann simulations to macroscopic models to empirical relationships). The various modeling approaches are necessary due to the lack of both in-situ experimental transport data and ex-situ material characterization. For a cell-level model, a macroscopic description of the DM provides the optimum balance between computational complexity and adequate physical description. Models of this sort rely on experimental data or results from more-detailed numerical investigations to determine the correct parameter functionalities. They also do not require knowledge of the detailed microstructure including its heterogeneous chemical interactions, which are difficult to describe in detail.

In general, the main point of DM models is to determine the transport parameters (*e.g.*, effective diffusion coefficients and permeabilities) as a function of operating conditions and

material properties. This is typically done by calculating a saturation or liquid pore-volume fraction using relationships such as the Leverett *J*-function [5-9], and then using the saturation to modify the intrinsic or dry-medium transport properties using relations like those of Corey [10], (Brooks-Corey) [11], Van Genuchten [12], or Bruggemann [13-15]. The more intricate pore-level modeling [16-24] has allowed the calculation of various transport properties from a handful of statistical structural properties such as pore- and throat-size distributions, porosity, and bulk-transport measurements including saturated permeabilities. While these models can provide some fundamental understanding of water percolation and movement, they are limited by a lack of measurements of the nonuniform chemical (i.e., wettability) distribution at the pore level. Although limited, the knowledge gained by these microscopic models can be used to refine more macroscopic models that can meet the runtime constraints for full-cell modeling.

Historically, describing the DM has been dependent on overall layer performance in a PEFC. However, recently several groups have begun to gain the expertise and apparati to study some of the material properties such as hydrophilic and hydrophobic pore-size distributions (PSDs) and capillary pressure versus saturation curves [8, 25-34]. These curves have been measured under a variety of conditions including compression and hydrophobic loading. Although ex-situ and equilibrium measurements, these studies allow for more detailed information than previously obtained and provide the basis for the next generation of macroscopic DM models.

The experimental findings include the fact that GDLs do not spontaneously imbibe or drain water, meaning that they exhibit a hysteresis between injection and drainage curves [30, 35-37]. This was originally shown by Benziger *et al*. [35], and it has been ascribed to the fact that GDL surface roughness and internal morphology cause a contact-angle hysteresis, which can also be explained through the different physics that govern injection versus drainage phenomena [38].

Other studies have tried to measure the tortuosity of the DM for gas-phase diffusion with some success [14, 39, 40]. Finally, Ziegler and Gerteisen [41] have shown that gas and not liquid is the wetting fluid in treated GDLs, which is expected due to their hydrophobicity and intermediate wettability.

In addition to ex-situ analyses, neutron [42-45] and other imaging techniques [46-49] have begun to allow one to see the in-situ DM water profiles with increasingly better resolution. These results clearly demonstrate complex water profiles, that have only begun to be compared to simulation predictions [50]. The origin of these profiles is due to the complex nature of both the material heterogeneities as well as phenomena such as phase-change-induced (PCI) flow where water moves due to phase transitions. For example, water evaporating and condensing along a temperature gradient can have a large impact on the cell performance [51-59], or similarly, during shutdown in a cold-environment, water is predicted and shown to move due to freezing [60-62]. Thus, a valuable and predictive macroscopic model must be able to handle changes in the chemical and physical DM structure along with the various dominant transport phenomena.

In this paper, the impact of DM wettability on PEFC performance under various operating conditions will be investigated. The key is to understand the experimental evidence through mathematical modeling. This paper sets forth an improved, self-consistent DM transport model, which is based on a previous model [63], but updated to incorporate the recent experimental characterizations mentioned above. Using this model, some limiting-case scenarios and sensitivity studies for the DM are accomplished, marking one of the first times that the direct capillary-pressure versus saturation measurements are used in simulations. In addition,

multilayer DM are examined, with a focus on the role of the MPL, something that is still not totally understood.

Updated Porous-Medium Model and Modeling Methodology

Governing transport equations.—The governing transport equations and physics are well known [1, 3]. For transport phenomena in the gas-phase, the Stefan-Maxwell multicomponent transport equations are used,

$$\nabla x_i = -\frac{x_i}{RT}\left(\overline{V}_i - \frac{M_i}{\rho_G}\right)\nabla p_G + \sum_{j\neq i}\frac{x_i\mathbf{N}_j - x_j\mathbf{N}_i}{c_T D_{i,j}^{\text{eff}}} - \frac{\mathbf{N}_i}{c_T D_{K_i}^{\text{eff}}} \tag{1}$$

where one of the equations is dependent on the others since the sum of the mole fractions is unity. In the above equation, R is the ideal gas constant, T is the absolute temperature, p_G and ρ_G are the pressure and density of the gas phase, respectively, and $\mathbf{N}_i$, $\overline{V}_i$, x_i, and M_i are the molar flux, molar volume, mole fraction, and molar mass of species i, respectively. The first term on the right side of equation 1 accounts for pressure diffusion and is often neglected, although it could be important on the anode side of the cell due to the large difference in molar mass between hydrogen and water.

In the second term, c_T is the total concentration or molar density of all of the gas species, and $D_{i,j}^{\text{eff}}$ is the effective binary interaction parameter between species i and j; by the Onsager reciprocal relationships, $D_{i,j}^{\text{eff}} = D_{j,i}^{\text{eff}}$. The effective diffusion coefficient is defined as

$$D_{i,j}^{\text{eff}} = \frac{\varepsilon_G}{\tau_G} D_{i,j} = \varepsilon_G^n D_{i,j} \tag{2}$$

where ε_G and τ_G are the volume fraction and tortuosity of the gas phase, respectively. As shown in the equation, the ratio is often expressed as a function of the gas-phase volume fraction alone. Often, a Bruggeman-type relation is used where n = 1.5; however, recent microscopic simulations and experimental studies have suggested that the value is closer to between 2 and 5 for typical GDLs [5, 14, 19, 20, 24, 39, 40, 64]. Although, it should be noted that some of these studies change the volume fraction by compression, which alters the pore network and is different than examining a change in tortuosity and volume fraction due to pore filling. In this paper, a Bruggemann expression is used, although, as discussed below, other functional relationships and forms are examined. There is a need to measure experimentally the gas-phase tortuosity as a function of liquid saturation.

The third term on the right side of equation 1 accounts for Knudsen diffusion, where $D_{K_i}^{\text{eff}}$ is the effective Knudsen diffusion coefficient of species *i*, and is made effective in the same manner as in equation 2. The Knudsen diffusion coefficient is a function of the pore radius through which it travels

$$D_{K_i} = \frac{2\bar{r}_K}{3}\left(\frac{8RT}{\pi M_i}\right)^{\frac{1}{2}} \tag{3}$$

where $\bar{r}_K$ is the average Knudsen radius. From an order-of-magnitude analysis, Knudsen diffusion is significant when the pore radius is less than about 0.5 μm, which occurs in MPLs, catalyst layers, and, to a lesser extent, in highly-saturated GDLs. Finally, the third term represents interactions between the gas species.

The Stefan-Maxwell equations in equation 1 are referenced to that of the laboratory reference frame *(i.e.*, stationary), which allows for the Stefan-Maxwell equations to account for not only

diffusive fluxes but also convection. However, a momentum equation is required to determine the pressure change. For DM modeling purposes, the resulting momentum equation reduces to Darcy's law

$$\mathbf{v}_{\mathrm{G}} = \frac{\sum_{i \neq s} M_i \mathbf{N}_i}{\rho_{\mathrm{G}}} = -\frac{k_{\mathrm{G}}}{\mu_{\mathrm{G}}} \nabla p_{\mathrm{G}} \tag{4}$$

where v_G, μ_G, and k_G are the mass-averaged velocity, viscosity, and effective permeability of the gas phase, respectively.

If a DM is not filled with any liquid, single-phase flow exists and the transport properties are more uniform throughout the medium, assuming that the structure of the medium does not change. Specifically, in the absence of any residual liquid saturation, the gas-phase volume fraction, ε_G, is equal to the porosity of the medium, ε_o, and the effective permeability, k_G, is equal to the saturated permeability, k_{sat}, which depends only on the microstructure and not on the fluid. Both of these values are typically known through ex-situ measurements. However, if liquid water does exist in the DM, so does two-phase flow. For this case, the gas-phase properties are adjusted to account for the presence of the liquid,

$$\varepsilon_G = \varepsilon_o (1 - S) \tag{5}$$

and

$$k = k_r k_{sat} \tag{6}$$

where S is the saturation or volume of pore space filled by liquid, and k_r is the relative permeability of the medium. Similarly, $D_{K_i}^{\mathrm{eff}}$ is also effected by liquid water since it depends on

the pore sizes through which gas flows. Overall, to describe transport in the DM with two-phase flow requires knowledge of the saturation and related transport properties.

Before describing the two-phase model, one should mention that liquid movement through the DM is also adequately modeled with Darcy's law

$$\mathbf{N}_{\mathrm{L}} = -\frac{k_{\mathrm{L}}}{\overline{V}_{\mathrm{w}}\mu_{\mathrm{L}}}\nabla p_{\mathrm{L}} \tag{7}$$

where the subscripts L and w stand for liquid and water, respectively. In the above expression, k_{L} is also a function of a relative permeability and the saturated permeability as in equation 6.

Finally, DM conduct electrons and heat, which can be modeled by Ohm's and Fourier's laws,

$$\mathbf{i} = -\sigma\nabla\Phi \tag{8}$$

and

$$\mathbf{q} = -k_{\mathrm{T}}\nabla T \tag{9}$$

respectively, where q is the heat flux, i is the current density, σ is the electronic conductivity, Φ is the electrical potential, and k_{T} is the average thermal conductivity. Typically, heat conduction dominates convection for DM thermal transport [52].

From the above governing equations, the required dependent parameters are the porosity/tortuosity corrections (equations 2 and 5), the liquid- and gas-phase permeabilities (equation 6), the average Knudsen radius (equation 3), and the thermal and electrical conductivities (equations 9 and 8), respectively). All but the last two are expected to change significantly with increased saturation, and this requires a two-phase-flow approach as described below.

Two-phase flow.— One key for any macroscopic model is the determination of the correct transport properties, as noted above. As previously described [63], our method is to use a cut-and-random-rejoin bundle-of-capillaries model. Although this model is not correct on the local, pore-scale level, it is believed that it contains enough description to remain valid at the macroscopic, layer-scale level; it provides a balance between material and physics descriptions and numerical simplicity and robustness. Furthermore, the model is entirely self-consistent. In the previous model, a continuous PSD is used along with a two-point discrete contact-angle distribution (CAD). In other words, single hydrophilic and hydrophobic angles are used, which, along with Nam and Kaviany [5], represented the first modeling and concept of mixed or nonhomogeneous wettable pores. In the model described herein, a continuous distribution is used. The ability to use the distribution stems from advancements in experimental techniques. While the previous model depends on fitting the various parameters to tangential data such as overall flow through a DM, it is now possible for the direct measurement of capillary-pressure versus saturation curves using various contact and equilibrium methods [8, 25-34]. The proposed procedure is similar to that of Cheung *et al*. [28], although they use a continuous CAD but a discrete PSD.

The concept is to utilize a component that is related to the material structure and one that is related to its chemical nature. The use of two continuous distributions also allows for detailing impacts of intermediate wettability and not necessarily saying something is definitively hydrophobic or hydrophilic. In all cases, water is the wetting fluid of the DM. Using two continuous distributions, an example property, Y, will be given by

$$Y = \iint \Psi(\theta) Y(r) V(r) \mathrm{d}r\mathrm{d}\theta = \int_0^{90} \Psi(\theta) \int_0^{r_c} Y(r) V(r) \mathrm{d}r\mathrm{d}\theta + \int_{90}^{180} \Psi(\theta) \int_{r_c}^{\infty} Y(r) V(r) \mathrm{d}r\mathrm{d}\theta \qquad (10)$$

where $V(r)$ is the normalized volume of pores of radius r (the structural component), and $\Psi(\theta)$ is the normalized number of pores with contact angle θ (the chemical component), and $Y(r)$ represents the weighting factor and any constants for the specific property. For numerical ease, the integral is broken into two with a transition at 90°. This value is chosen since the integration is done with respect to the critical radius, or that of the incipiently filled pore, which is given by [65, 66]

$$r_c = -\frac{2\gamma\cos\theta}{p_{\mathrm{L}} - p_{\mathrm{G}}} = \frac{2\gamma\cos\theta}{p_{\mathrm{C}}} \tag{11}$$

where p_{C} is the capillary pressure and γ is the surface tension of water. The above equation is valid for cylindrical pores, which do not occur in the fibrous DM materials. However, the measurement of the PSD similarly assumes cylindrical pores and any error in the use of the mathematical construct is assumed to be small due to the use of capillary-pressure data for the fitting of the CAD. In equation 10, the integration limits with respect to the critical radius change due to the way in which the pores fill between those less than 90° (hydrophilic) and those above (hydrophobic), and is in agreement with environmental microscopy images [41]. Equation 10 clearly demonstrates that the impact of both pore size and wettability are intricately linked and cannot necessarily be separated out; it is a combined effect.

The PSD is fit using a series of log-normal distributions (typically two per layer)

$$V(r) = \sum_k f_{r,k} \left\{ \frac{1}{r s_k \sqrt{2\pi}} \exp\left[-\left(\frac{\ln r - \ln r_{\mathrm{o},k}}{s_k \sqrt{2}} \right)^2 \right] \right\} \tag{12}$$

where $V(r)$ is the normalized volume of pores of radius r, $r_{\mathrm{o},k}$ and s_k are the characteristic pore size and spread of distribution k, respectively, and $f_{r,k}$ is the fraction of the total distribution

made up of distribution *k*, where the $f_{r,k}$'s sum to unity. A log-normal distribution is used because it fits the data, is normalized, and allows for analytic expressions. For reference, the average pore size is given by

$$\bar{r} = \frac{\sum_k \frac{f_{r,k}}{r_{o,k}} \exp\left[\frac{s_k^2}{2}\right]}{\sum_k \frac{f_{r,k}}{r_{o,k}^2} \exp\left[2s_k^2\right]} \tag{13}$$

An example PSD fit for an SGL24BC DM with both a GDL and MPL is shown in Figure 1a. The data were obtained using mercury-intrusion porosimetry [25]. Two terms are used each for the GDL and MPL PSDs; the values are given in Table I. The total PSD of the composite structure can be calculated from the individual layer PSDs by

$$V(r) = \frac{V(r)\big|_{GDL} l_{GDL} \varepsilon_{o,GDL} + V(r)\big|_{MPL} l_{MPL} \varepsilon_{o,MPL}}{l_{GDL} \varepsilon_{o,GDL} + l_{MPL} \varepsilon_{o,MPL}} \tag{14}$$

where *l* is the layer thickness. As seen in the figure, the fit is very good and describes all of the pores. Additionally, the natural breakdown of the two fits and their individual PSDs, shown in Figure 1b, demonstrate that the GDL is mainly composed of the larger macropores with the MPL composed of the micro and mesopores. This is in agreement with previous analyses and PSDs of carbon paper GDLs [28, 31, 34]. Furthermore, the PSD of the MPL is very wide, which allows for less flooding and more control over water management [77, 78]. On a pore-size basis, there is a significantly larger number of small pores located in the MPL than the GDL, but this changes if one examines the relative pore volumes (see equation 14). Some of the largest pores can be ignored since these typically result from the cracks during sample preparation and loading and do not represent real DM pores.

As a side note, one can also measure separate hydrophilic and hydrophobic PSDs by changing the wetting fluid [25, 26, 31, 34]. However, their interpretation is often confused and can lead to non-physical pore sizes for one of the distributions [26]. This is not too surprising since the PSD and CAD are coupled as seen in equation 10, and the impact of the detailed microstructure becomes more important (e.g., pores that have mixed wettability or are dominated by pore throats of a given kind). While measuring the hydrophilic and hydrophobic PSDs can reveal some characteristics (e.g., the MPL is hydrophobic), a more rigorous microscopic model is needed for the actual penetration experiment for the data to be quantitatively meaningful. It is more desirable to use the saturation versus capillary pressure data that is now available rather than the hydrophilic and hydrophobic porosimetry data.

To model the CAD, a normal distribution is used [28, 79]

$$\Psi(\theta) = \sum_n f_{\theta,n} \left\{ \frac{1}{\sigma_n \sqrt{2\pi}} \exp\left[-\frac{1}{2} \left(\frac{\theta - \theta_{o,n}}{\sigma_n} \right)^2 \right] \right\} \tag{15}$$

where $\theta_{o,n}$ and σ_n are the characteristic contact angle and deviation of distribution *n*. There is no independent measurement than can be used to determine these parameters. For example, surface contact angles are not representative of those within the medium since they are dominated by water penetration, roughness, and other surface effects [33, 37]. If the detailed geometry and pore space is known including Teflon distribution, one could guess at a CAD; however, these distributions are unknown. Even if one guesses the distributions, they only represent part of the chemical nature of the DM since, due to the DM intermediate wettability caused by the constituent Teflon and graphite moieties, pore necks, fiber orientation, and other

related effects [38, 80]. Since there is no independent measurement of the CAD, it is best determined by fitting the available capillary pressure – saturation relationships.

Using equation 10 for saturation, where a pore is filled or empty depending on how it relates to the critical radius (equation 11), one gets

$$S^* = \int_0^{90} \Psi(\theta)\left\{\sum_k \frac{f_{r,k}}{2}\left[1+\operatorname{erf}\left(\frac{\ln r_c - \ln r_{o,k}}{s_k\sqrt{2}}\right)\right]\right\}d\theta + \int_{90}^{180} \Psi(\theta)\left\{\sum_k \frac{f_{r,k}}{2}\left[1-\operatorname{erf}\left(\frac{\ln r_c - \ln r_{o,k}}{s_k\sqrt{2}}\right)\right]\right\}d\theta$$

$$= \int_0^{90} \sum_n f_{\theta,n}\left\{\frac{1}{\sigma_n\sqrt{2\pi}}\exp\left[-\frac{1}{2}\left(\frac{\theta-\theta_{o,n}}{\sigma_n}\right)^2\right]\right\}\left\{\sum_k \frac{f_{r,k}}{2}\left[1+\operatorname{erf}\left(\frac{\ln\left(-\frac{2\gamma\cos\theta}{p_C}\right)-\ln r_{o,k}}{s_k\sqrt{2}}\right)\right]\right\}d\theta \qquad (16)$$

$$+ \int_{90}^{180} \sum_k \ldots$$

where the last term is left off for brevity and erf is the error function. Typically, the above integration is done using a 20-term Gauss-Legendre integration method [79] to increase computational speed. Also, this method allows for implementation in codes where one must define set integration points (e.g., computational-fluid-dynamics). To increase numerical accuracy, end limits of ±4 standard deviations (σ_n) are used. If one wants to use separate hydrophilic and hydrophobic PSDs, this can be accomplished by putting the hydrophilic PSD in the first term and the hydrophobic PSD in the second one. The experiments and hydrology literature also state that there exists an irreducible or residual liquid saturation, S_r. This saturation is distributed in isolated pockets within the DM, and thus the saturation given by equation 16 can be scaled

$$S = S_r + S^*(1 - S_r) \qquad (17)$$

Using the fits from Figure 1 and Table I for the SGL10BA (similar GDL, but no MPL as in Figure 1) and Toray GDLs, the CADs were fit to the cycled capillary pressure versus saturation data from the literature [28, 29, 34, 80] as shown in Figure 2. From the data, one can see that both an irreducible liquid saturation and a large hysteresis exist. The residual saturation is expected since water is the nonwetting fluid in GDLs and, due to the fibrous nature and non cylindrical pores, corner flow of gases will exist and liquid droplets can become entrapped [81, 82].

The Toray fits in Figure 2 compare our previous two-point approach (dotted line) with the improved continuous approach (solid line) herein. The comparison demonstrates that the improved model is much more accurate and smooth (especially around 90°), which should help numerical stability and convergence. In terms of the SGL fits, both the drainage and filling curves fit well, and can be improved further by adding a second term in the CAD, which will help the end segments of the curve. Also given in Figure 2 are the drainage and filling curves for a SGL GDL with 5 wt-% Teflonization. The increase in the hydrophobic treatment causes a shift of the curves to the right as expected [34, 80]. This shift causes the angle in the CAD to also shift to higher values with around an increase of 5° for the 5 wt-% Teflon-content increase. This correlation is not necessarily general due to the nature of the cosine function (it becomes weaker the further from 90°) and also the GDL material; thus, separate capillary pressure – saturation curves should be fit if available. Also, the PSD can shift due to the addition of Teflon, something that is not changed in Figure 2 and becomes more prominent with higher loadings [39]. It is noteworthy that the fit for the Teflonized SGL GDL utilizes a narrower CAD, which one might expect due to the smoothing that the Teflon could have by filling in pore surface space

and junctions. Mathematically, the narrower distribution means that one could use a single value without introducing too much error and therefore gain significant computational speed.

A mention should be made concerning hysteresis in DM materials. As seen in Figure 2, the curves exhibit a hysteresis between injection and drainage, which demonstrates preferential wetting of the pores, the importance of history, and that the GDL pores exhibit intermediate wettability. In other words, typical GDLs want to stay in the condition they are in (i.e., if they are wet it is energetically favored to remain wet) and will not spontaneously imbibe or drain water. This is in agreement with several groups that note that a certain pressure is necessary to overcome the surface resistance, but when it has, the water flows and easily through the layer [35, 80, 83]. In addition, the hysteresis is in agreement with surface and fiber contact-angle hysteresis seen with these materials [30, 37]. The hysteresis shown in Figure 2 is for the full range of saturation, and it is of interest to determine the tie lines between the curves since typically the DM are not operated anywhere close to full flooding. The simplest way to do this is just to scale the injection or drainage curve. For injection to drainage and vice versa, this can be done by

$$Y = Y_0 Y^* \tag{18}$$

and

$$Y = Y_0 + Y^*\left(1 - Y_0\right) \tag{19}$$

respectively, where Y_0 is the value of the property at which one goes from injection to drainage, and Y^* is the value of the property using the equations derived above with the drainage CAD. For saturation, the drainage to injection is as given in equation 19 (i.e., the turning point becomes like a residual saturation), and the injection to drainage using the residual saturation becomes

$$S = S_{\mathrm{r}} + S^{*}\left(S_{0} - S_{\mathrm{r}}\right) \tag{20}$$

To examine these expressions, the model was run for various injection to drainage cases and compared to the data of Gostick et al. [38] The comparison is shown in Figure 3, where the GDL used was a wet-proofed Toray paper. To better capture the injection behavior, a bimodal CAD was used, and the angles are higher than the unteated Toray sample in Figure 2, which agree with the lower saturations near a zero capillary pressure. The data and model for the full-saturation-range curves demonstrate good agreement, and it can be tuned better by adding some larger pores to the Toray PSD (not shown). In terms of the intermediate saturation hysteresis, the simple scaling method does capture most of the effects. The model does overpredict and underpredict the saturation values near drainage curve, and this error could be lessened by a more complex averaging method, although it is debatable how much empiricism such a method requires. In addition to the injection to drainage curves, a sample drainage to injection tie line is also given in Figure 3.

While the DM exhibit hysteresis which can be captured by the model, there is an issue of its actual importance in operating cells. The hysteresis presented is caused when one moves from water injection to drainage or vice versa.

In an operating cell, one does not expect to enter water-drainage conditions and instead it is more similar to an injection of water from the catalyst layer where the flowrate of the liquid is varied. In other words, the net flux of water is always the same (away from the electrode) under humidified conditions, thus drainage does not occur. The exception to this perhaps is during cell drying or with humidity gradients that cause a change in the water-flux direction. However, the hysteresis could be important on the pore-scale level under dynamic operation.

Before proceeding to discuss the transport properties, it is worthwhile to examine how the capillary pressure – saturation relationship changes by changing the CAD and PSD properties. To examine these effects, the PSD and CAD parameters are varied and different saturations are calculated using equation 16. The baseline case is a Toray PSD and a single CAD that yields a value of 0.5 at a 0 capillary pressure. The results of the study are shown in Figure 4.

From Figure 4a it is readily apparent that changing the CAD can have a very significant impact on the curves, with larger distributions causing gentler increases in the saturation with capillary pressure. However, the shape of cosine function that is in equation 16 means that changes and values around 90°, such as those in Figure 4a, will result in more significant changes to the curve. As one moves away from 90°, the effect of the CAD width becomes less significant. This is shown in Figure 4b where the most significant changes due to CAD width occur with 90°. The impact of the cosine dependence is also magnified with smaller pores, as shown in Figure 4b, which is due to the fact that the chemical nature and surface of the pore begins to dominate its uptake behavior with smaller pores (see equation 11). Finally, Figure 4b also suggests that changes towards larger contact angles are slightly more important than with lower contact angles, which is mainly due to the fact that water is the wetting fluid and pore filling is opposite between hydrophilic and hydrophobic pores.

Figure 4a also demonstrates that changing the width of the PSD seems to change the tails of the capillary pressure – saturation curve, and is not as significant as changing the CAD. On a percentage basis, the changes to the PSD and CAD are similar. Figure 4c examines the PSD width in more detail, showing that its effect is relatively small as expected, and again is more important for smaller rather than larger pores.

While the capillary pressure – saturation relationship is key and measureable, it is an equilibrium measurement and not related to transport. Thus, while it does give the effective gas-phase volume fraction (see equation 5), it does not directly relate to the transport properties needed above. This is why we fit the relationship as we do, instead of just using a hyperbolic tangent, i.e., it allows us to determine the transport-property expressions. To calculate these relationships, the CAD and PSD that are fit to data are used as in equation 10 with the appropriate weighting functions (e.g., proportional to r^2 for water flow) and statistical arguments to determine the various transport properties [63]. This approach does assume local equilibrium and that the capillary pressure – saturation relationship is independent of GDL thickness (i.e., it is the same everywhere).

Doing these manipulations results in expressions for the relative permeability of the gas and liquid (see equation 6) of

$$k_{r,\mathrm{L}} = S_e^2 \frac{\begin{array}{c}\int_0^{90} \Psi(\theta)\left\{\sum_k \frac{f_{r,k}}{2} r_{\mathrm{o},k}^2 \exp\left[2s_k^2\right]\left[1+\operatorname{erf}\left(\frac{\ln r_{\mathrm{c}} - \ln r_{\mathrm{o},k}}{s_k\sqrt{2}} - s_k\sqrt{2}\right)\right]\right\}\mathrm{d}\theta + \\ \int_{90}^{180} \Psi(\theta)\left\{\sum_k \frac{f_{r,k}}{2} r_{\mathrm{o},k}^2 \exp\left[2s_k^2\right]\left[1-\operatorname{erf}\left(\frac{\ln r_{\mathrm{c}} - \ln r_{\mathrm{o},k}}{s_k\sqrt{2}}\right) - s_k\sqrt{2}\right]\right\}\mathrm{d}\theta\end{array}}{f_{\mathrm{HI}}\left\{\sum_k f_{r,k} r_{\mathrm{o},k}^2 \exp\left[2s_k^2\right]\right\} + \left(1-f_{\mathrm{HI}}\right)\left\{\sum_k f_{r,k} r_{\mathrm{o},k}^2 \exp\left[2s_k^2\right]\right\}} \tag{21}$$

and

$$k_{r,\mathrm{G}} = (1-S)^2 \frac{\begin{array}{c}\int_0^{90} \Psi(\theta)\left\{\sum_k \frac{f_{r,k}}{2} r_{\mathrm{o},k}^2 \exp\left[2s_k^2\right]\left[1-\operatorname{erf}\left(\frac{\ln r_{\mathrm{c}} - \ln r_{\mathrm{o},k}}{s_k\sqrt{2}} - s_k\sqrt{2}\right)\right]\right\}\mathrm{d}\theta + \\ \int_{90}^{180} \Psi(\theta)\left\{\sum_k \frac{f_{r,k}}{2} r_{\mathrm{o},k}^2 \exp\left[2s_k^2\right]\left[1+\operatorname{erf}\left(\frac{\ln r_{\mathrm{c}} - \ln r_{\mathrm{o},k}}{s_k\sqrt{2}}\right) - s_k\sqrt{2}\right]\right\}\mathrm{d}\theta\end{array}}{f_{\mathrm{HI}}\left\{\sum_k f_{r,k} r_{\mathrm{o},k}^2 \exp\left[2s_k^2\right]\right\} + \left(1-f_{\mathrm{HI}}\right)\left\{\sum_k f_{r,k} r_{\mathrm{o},k}^2 \exp\left[2s_k^2\right]\right\}} \tag{22}$$

respectively, where f_{HI} is given by

$$f_{\mathrm{HI}} = \sum_n \frac{f_{\theta,n}}{2}\left[1+\mathrm{erf}\left(\frac{90-\theta_{o,n}}{\sigma_n\sqrt{2}}\right)\right] \tag{23}$$

and an effective saturation is used for the liquid relative permeability[5, 66]

$$S_e = \frac{S-S_r}{1-S_r} \tag{24}$$

The above expressions nominally yield the relative permeabilities as a function of the capillary pressure. For comparison sake, a power-law arrangement is often used for the relative permeability as a function of saturation (i.e., the first term in equations 21 and 22) [1, 3]. This relationship is shown in Figure 5 for the Toray and SGL GDLs, although the dotted curves are for comparison only and not fit to the simulation results. The figure clearly shows that there is a substantial predicted difference between the two materials. This difference is something that a single power-law exponent would be unable to determine. The Toray paper demonstrates close to a cubic dependence on saturation for the relative permeabilities whereas the SGL shows a much higher-order dependence. .The reason for the much larger dependence of the SGL is due to the much wider PSD. A wide PSD results in a breakdown of the bundle-of-capillaries model because the pore space becomes too ill-defined and comprises too many different-sized pores. This highlights one of the drawbacks of the presented methodology in that for very wide PSDs (s > 0.7), the calculation of the relative permeability results in an effective permeability that is too low, especially for the gas phase. Thus, simulations using this approach can result in more gas-phase pressure drop and flow resistance than one would probably expect in the actual system. For this reason, it is recommended that a 5^{th}-order dependence is set to be the maximum that can be obtained; the order dependence of around 2 to 5 agrees with recent pore-network modeling

studies [19-21]. It should be noted that for this paper, the differential impacts of changing properties is being explored and not the exact magnitude.

The use of the irreducible saturation in equations 21 and 22 is demonstrated in Figure 5 in that the gas-phase relative permeability does not reach a value of 1. Thus, the curves look somewhat opposite what one would normally expect in porous media. The reason is that for this system, the gas is the wetting fluid and the water the nonwetting one. Furthermore, the liquid is expected to exist more as droplets and the gas as a continuous film that can flow around the droplets [41], thus the relative permeability for the gas phase approaches, but does not reach, zero.

While Figure 5 displays the relative permeabilities, Figure 6 shows the calculated effective permeabilities for the two GDLs as a function of the capillary pressure (note that the saturated or absolute permeability of the SGL GDL is about three times larger than that for the Toray paper (see Table I)). Both curves exhibit a relatively steep drop in permeability over a relatively small range of capillary pressure, which is not surprising due to the shape of the capillary pressure – saturation profile (Figure 2). The SGL curve is more asymmetric between the two permeabilities and the liquid effective permeability is broader. This is caused by the above-mentioned effects including the wider PSD and CAD for the SGL material.

The final transport property that varies as a function of the liquid and gas volume fractions is the average Knudsen radius (see equation 3). This radius is determined in a similar manner to the permeability and is related to taking integrals with respect to the transport property and the flux, however, with the integration limits reversed since the gas-filled pores are of interest [63]. Thus, the average Knudsen radius is essentially the unfilled volume-averaged pore radius. Doing the required mathematical manipulations yields an expression for the average Knudsen radius of

$$\bar{r}_K = \frac{\int_0^{90} \Psi(\theta)\left\{\sum_k \frac{f_{r,k}}{2} r_{o,k} \exp\left[\frac{s_k^2}{2}\right]\left[1-\operatorname{erf}\left(\frac{\ln r_c - \ln r_{o,k}}{s_k\sqrt{2}} - \frac{s_k}{\sqrt{2}}\right)\right]\right\}d\theta + \int_{90}^{180} \Psi(\theta)\left\{\sum_k \frac{f_{r,k}}{2} r_{o,k} \exp\left[\frac{s_k^2}{2}\right]\left[1+\operatorname{erf}\left(\frac{\ln r_c - \ln r_{o,k}}{s_k\sqrt{2}}\right) - \frac{s_k}{\sqrt{2}}\right]\right\}d\theta}{1-S} \quad (25)$$

The curves for SGL and Toray are shown using the right axis in Figure 6. It is clear that as the pores become filled, the average radius will increase slightly in the hydrophilic pore range and decrease more significantly in the hydrophobic range due to the way in which the pores fill (i.e., small hydrophilic to large hydrophilic to large hydrophobic to small hydrophobic). This is seen in the Toray analysis in Figure 6 but not as much in the SGL curve due to the lower amount of hydrophilic-type pores and the wide PSD. The overall analysis is flawed due to the assumption of cylindrical pores, but it allows for at least a way to account for some of the gas – pore-wall interactions, which become significant in MPLs.

While all of the transport properties have been discussed, a couple of points should be noted. First, the vapor pressure is expected to be a function of water content in the medium. This can be calculated by combing the Young-Laplace equation with the Kelvin equation [65], yielding

$$p^{\text{vap}} = p_o^{\text{vap}} \exp\left(\frac{p_C \bar{V}_w}{RT}\right) \quad (26)$$

where p_o^{vap} is the uncorrected vapor pressure of water. This equation also allows one to assume equilibrium between water vapor and liquid and have continuous functions of their concentrations. Second, the above analysis has ignored a couple of issues such as GDL anisotropies [68, 84, 85] and compression [8, 86, 87], which can somewhat be accounted for by using average properties and capillary pressure – saturation curves measured under operating-

type conditions. Overall, the above methodology allows for one to go beyond simple curve fits and thus can provide educated guesses to the impact of various properties.

Governing conservation equations and boundary conditions.—The governing transport equations and the two-phase flow model for their parameters are discussed above. To complete the modeling of a DM, the conservation equations and boundary conditions are required. These relationships for the cathode DM being simulated herein are shown in Figure 7. A conservation equation is required for each species. The only reaction that occurs within the DM is that of water phase change, and, due to the intimate contact between liquid and vapor, it is assumed that the two are in equilibrium. This means that there is only an overall water balance and that equation 26 is used to relate the water-vapor partial pressure with the liquid pressure in the DM. Also, the focus of this study is on gas and liquid transport, and thus the current-density equations are ignored. For the energy equation, ΔH_{evap} is the heat of vaporization of water.

Figure 7 also shows the boundary conditions used in this study. These boundary conditions are relatively straightforward since we are only interested in examining how transport through the DM changes. In reality, the DM boundary conditions are coupled to the other layers and also are complicated by the existence of catalyst layers, ribs and channels, etc. To account for the effects of the ribs and channels, an effective DM-length multiplier for a rib-to-channel ratio of 1:1 is used (i.e., 1.6x) as described by Weber [88]. Furthermore, the interface between the flow-field gas channel and the GDL can become controlling and is complex [37, 47, 83, 89], although by examining only steady-state behavior, the transient and droplet aspects can be more-or-less ignored.

The boundary conditions can be described as follow. For the energy equations, set temperatures are used at both boundaries (typically 70°C for this work). The gas composition in the gas channel is taken to be known (typically fully humidified air). Nitrogen crossover through the membrane is ignored. The gas pressure is set equal to the known value in the gas channel (1 bar). The liquid pressure at the boundary is set by the determined breakthrough capillary pressure or, in other words, when the capillary pressure when the saturation becomes larger than residual saturation and water can flow (i.e., nonzero effective permeability), e.g., 1 kPa for base SGL GDL. This capillary-pressure boundary condition has a lower value of zero when there is two-phase flow, which corresponds to a DM with some hydrophilic-type pores (e.g., Toray paper). Also, this boundary condition is expected to increase with increased DM hydrophobic treatment and agrees with experimental breakthrough pressure analysis and GDLs having intermediate wettability.[35, 80] The water flux from the catalyst layer is taken to be known and is a varied parameter (in full-cell simulations, this flux is related to the water production and net water transport through the membrane). Finally, either the oxygen flux or concentration is taken to be known at the catalyst layer; in either case, the oxygen flux can be related to a current density through Faraday's law

$$\mathbf{N}_{O_2} = \frac{\mathbf{i}}{4F} \tag{27}$$

where F is Faraday's constant.

The above governing equations are discretized in 1-D (i.e., anisotropy is ignored) and solved numerically as a boundary-value problem using BAND(*j*) [90].

Results and Discussion

The above model can be used to explore the effects of the CAD and the measured data on flow through the DM. One method to examine a performance signature for a GDL is to analyze the resulting limiting current density on air [30, 40]. To keep the analysis simple, the highest possible mass-transfer limiting current is used, thus, the concentration of oxygen at the right or liquid-inlet side of the GDL (see Figure 7) is set equal to zero. Then, the limiting current density is determined from the oxygen flux using Faraday's law. For a GDL signature, this is done as a function of the total inlet water flux and the results are shown in Figure 8. It should be noted that this limiting current density ishould be higher than that in an operating PEFC since only DM mass-transfer losses are considered. Also, the limiting current density is due to diffusion and not convection in the gas phase, although this diffusion is limited by the saturation profile *see equation 2).

Several important conclusions can be reached from Figure 8. First, the limiting current density just due to mass-transfer effects for this GDL is high until one reaches very large flowrates. To put the x-axis in more familiar terms, the range given corresponds to a current density of milliamps to thousands of amps per centimeter squared. Obviously, the true limiting current in a cell is due to a combination of factors not the least of which are poor oxygen-reaction kinetics, ohmic losses, and mass-transfer losses in the catalyst layer. Furthermore, the SGL properties used are not for a compressed GDL and the rib/channel effects are taken into account only in an average sense. However, Figure 8 clearly demonstrates that mass-transfer limitations in the GDL are not caused by increased pressure due to increased liquid flowrate, unless the GDL has an orders-of-magnitude lower permeability. Also the results suggest that one might expect low GDL saturations in operation under ideal conditions where the GDL is

near its breakthrough pressure. The high permeability and porosity of typical GDLs results in liquid-water flowrate affecting performance only minimally, which is perhaps expected for a capillary-dominated flow. This small dependence is clearly shown by the flatness of all of the curves on the left side of the figure, i.e., where the water flux corresponds to expected operational flowrates. The flatness of the profiles indicates that the observed GDL mass-transfer limitations are controlled by surface and boundary interactions, not bulk transport, which has been assumed to be the case in some past simulations. Finally, these results also suggest that no-GDL limitations (e.g., oxygen transport to the reaction sites within the catalyst layer) are dominant in an operating PEFC.

Before examining other GDL limitations, it is of interest to examine a couple of different scenarios, which are also given in Figure 8. First is the question of the effect of pore size and wettability. Due to the wet-proofing process, one could expect that the larger pores are more hydrophobic on average than the smaller domains, which agrees with water and mercury PSD analyses [25]. Simulations were run by taking either the large or small branch of the PSD and combining them respectively with two different CADs. The results show that having more hydrophobic larger pores compared to the smaller ones results in an increase of the limiting current density, whereas the opposite results in a modest decrease. This result is explained by the fact that the larger pores account for more volume and, if they are more hydrophobic, then the saturation is lower for the same capillary pressure. Also, because there are fewer larger pores, and wettability has a smaller impact on them, the more hydrophobic large-pore curve is affected at lower liquid flowrates than the small-pore one. At very high water fluxes, the wettability difference between pores becomes irrelevant since all are filled and the same overall PSD is utilized.

Figure 8 also display the effect of putting very large holes into the GDL. This has been shown to increase performance [91]. The simulations, however, show that one would expect lower performance because the large holes would fill with water and thereby increase the GDL saturation and lower the oxygen diffusion. The apparent conflict between the simulation and experimental results is because the simulation only examines one issue, namely, that of water transport through the bulk GDL. In Figure 8, a liquid pressure at the channel or outlet side is assumed. However, Figure 4 shows that larger pores should result in a lower change in the capillary pressure. Indeed, one would expect the liquid exiting pressure to be lower due to the large holes providing an escape path for the liquid water. In addition, the very large pores might decrease the liquid percolation pathways (i.e., provide freeways for water to flow in). Thus, the overall saturation of the GDL may be less with the large pores due to its impact to provide water egress and pathways and alter the GDL – channel boundary.

To explore the boundary effect in more detail, simulations were run where the capillary-pressure boundary condition is varied. For these simulations, the oxygen partial pressure is calculated assuming oxygen and water fluxes corresponding to 2 A cm^{-2}. From Figure 8, the value of the water flux should not have a large effect in this range (it is around 2%), and comparisons of curves and effects will likewise remain valid for various oxygen fluxes. The simulation results are shown in Figure 9 for a variety of CADs for SGL GDLs. It should be noted that the channel oxygen partial pressure is 14 kPa. Not surprising, the capillary-pressure boundary condition has a very significant effect, especially over a small capillary-pressure range, which is in agreement with the shape of the capillary pressure – saturation curves for these materials (see Figure 2). This highlights the fact that liquid saturation and pressure can become limiting, with a zero oxygen partial pressure occurring at an average GDL saturation around 0.6.

However, most current simulations and some experimental ones [42] suggest that the water saturations do not reach such high levels under steady-state performance.

The curves in Figure 9 start from different points corresponding to the required breakthrough pressure. In reality, the capillary pressure at the boundary is a function of a variety of conditions including the breakthrough pressure, the operating conditions including temperature, gas flowrate, etc., the existence and effect of the channel walls and liquid in the channel, and other conditions; it is also expected to by dynamic with an increase for droplet formation, decrease for growth, and then ejection. In fact, Gostick et al. [80] have shown that there can be an oscillation of a magnitude around 2 kPa for the droplet emergence, growth, and detachment phenomena under static conditions at room temperature. Such an oscillation can be problematic depending on how close to breakthrough one is operating (i.e., where on the saturation curve). Furthermore, such oscillations might also occur internally at various interfaces. The dynamics of the system is an area that needs further exploration. Finally, it should be noted that the capillary-pressure values shown are average values (i.e., if there is a uniform reservoir or film of liquid at that pressure). Since most GDLs will have droplets and certain exit points, as well as operate dynamically, the local values of the capillary pressure will vary with time and location.

From Figure 9, changing the angle has a more significant direct impact than changing the distribution width. This is because it shifts the curve rather than just spreading it out. As noted above, increasing the GDL Teflon content shifts the saturation – capillary pressure curve to the right This shift increases performance up to the point where the change in breakthrough pressure, possibly PSD and porosity changes, and surface effects offset the performance gain. Changing the distribution width does change the pore filling (see Figure 4), which impacts how steep the dropoff is with the increased pressure. Overall, if one normalizes the results to the

breakthrough capillary pressure, the wider distribution gives the best performance range, which is perhaps more important.

From Figure 8 and Figure 9, it is clear that diffusion and not convection dominate the mass-transport limitations in DM. In other words, the capillary pressure does not change significantly in a DM. The key property that is necessary is then the effective diffusion coefficient as a function of capillary pressure or saturation, which is essentially determined by the exponent *n* in equation 2. As mentioned, this value has a range from pore-network modeling simulations and compression studies. To understand its impact on the performance here, a sensitivity analysis is accomplished. This analysis assumes that the tortuosity can be expressed as

$$\tau_G = \tau_{G,0}\varepsilon_G^n \tag{28}$$

where for Bruggemann, the values would be $\tau_{G,0} = 1$ and n = –0.5. The results of the analysis are shown in Figure 10. It is obvious that the more tortuous the pathway, the greater the impact. Furthermore, the impact on the partial pressure can be significant, although the other qualitative results examined in this paper remain valid. The exact dependence of the tortuosity on saturation needs to be quantitatively measured if possible.

It is also of interest to investigate the effect of that the MPL has on performance using the model. It is well known that MPLs increase PEFC performance [1, 92, 93]. In addition, experimental studies with MPLs have also lead to the idea that one function of the MPL is to reduce the injection sites for water from the catalyst layer to the GDL, which in turn reduces the saturation at breakthrough [21, 94]. To ascertain the impact of the MPL, simulations similar to those of Figure 9 are run with a DM composed of an MPL and GDL (i.e., SGL24AC) going from water inlet (catalyst layer) to outlet (channel). The simulation results are given in Figure 11

along with a some other cases as described below. Compared to the GDL-only analysis, the assumed water flux (i.e., related to 2 A cm^{-2}) has a more substantial impact due to the low MPL permeability, but it is still relatively minor and liquid-water transport through the GDL is again not limiting; the case comparisons remain valid. It should also be noted that MPL impact will also change depending on its thickness.

From Figure 11(a), it is apparent that the addition of the MPL is predicted to result in lower performance since the oxygen partial pressure reaching the catalyst layer decreases. This is not surprising since the MPL provides an added resistance to oxygen diffusion, which is significant due to the low porosity and thickness of the MPL. However, the analysis does not include any kind of beneficial effects in terms of utilization, increased temperatures, lower contact resistances, etc. that an MPL can provide; the focus is on the transport-phenomena aspects.

Figure 11(b) shows the capillary pressure at the water inlet (i.e. catalyst layer), where the sharp increase in curve slope is due to the rapid decrease in the gas-phase pressure when the DM is flooded. This metric can be thought of as the ability to better hydrate the membrane and force water from the cathode to the anode since higher capillary pressures would mean higher saturations in the catalyst layer next to the membrane and also that there is a higher liquid pressure which could help drive water transport through the membrane. For the former, one would expect that cell performance would be greater with MPLs and hydrophilic GDLs at low relative humidities and poorer at high relative humidities. This is in agreement with experimental data, where relative-humidity sweeps can help to develop a DM signature [25]. For the water-flux effects, the MPL influence is probably minimal for typical operating conditions since water flux is not that impactful on gas transport and newer membranes are much more resistive to liquid-water flow [95], also in agreement with some experimental data [92].

The inlet-capillary-pressure curve for the MPL is also remarkably flat until the GDL begins to flood at higher outlet pressures and a large enough water channel can exist across the MPL. The difference between the MPL and GDL-only curves in Figure 11(b) can be seen as the ability of the MPL to pressurize the water without flooding itself, as discussed above, and also its ability to smooth any pressure fluctuations. Thus, the response of a cell should be more stable when an MPL is used. Also, since the liquid-phase pressure drop occurs almost entirely within the MPL, GDL material-property changes become less significant cell-performance factors, as has been discussed before [77]. This smoothing function of the MPL begins to decline as the DM fills with water and there is substantial hydrodynamic contact across the MPL, thereby spreading out the pressure drop in the MPL instead of having it mainly confined to the MPL/GDL interface.

It is thought that an MPL allows for more water to travel in the vapor phase due to its low thermal conductivity and high hydrophobicity. To investigate this, simulations were run with a 2°C temperature gradient across the DM. Such a gradient is expected to increase the water flux in the vapor phase and result in phase-change-induced flow where the water vapor is now traveling down the temperature gradient (i.e., into the channel) and against the incoming oxygen [50, 96]. Such flow can also generate complex DM profiles and is expected to be detrimental to cell performance. This is in agreement with the simulation results in Figure 11 which show that the performance is decreased due to lower overall oxygen partial pressure unless the cell is nearly flooded. In this case, the benefits of water removal via phase-change-induced flow offset the detriments of the water-vapor-flux reversal. The ability of phase-change-induced flow to remove the liquid water is shown by the lower inlet capillary pressure in Figure 11(b).

All of the MPL effects so far have not really shown an increase in the oxygen partial pressure. The question is whether something is left unaccounted. Recently, Gostick et al. [94]

have shown that the GDL capillary pressure - saturation relationship is altered when measured with a MPL. They ascribe this effect to the MPL distributing the water into the GDL at discrete points rather than the more uniform and film-like water penetration expected by a catalyst layer (although the high in-plane permeabilities result in some water spreading out from the point source). They demonstrate that masking likewise causes a more hydrophobic-like response from the GDL with a higher breakthrough pressure and lower saturation at breakthrough. To study this possible effect, simulations were carried out by assuming that only a portion (60 %) of the MPL provides water to the GDL, with the rest having a very hydrophobic signature (i.e., an angle of 140° is used for the remaining 40%). Thus, the saturation response is scaled. This case, as shown in Figure 11, does provide for better oxygen transport at higher outlet capillary pressures and a lower propensity to flood. The discrete-point concept can be taken further by examining the response if one could manufacture the defect sites either by crack formation, perforation, or by adding hydrophilic pores to the MPL. Figure 11 shows this result where the scaled GDL saturation case is combined with the addition of 15% hydrophilic pores. This combination provides the best response in terms of partial pressure. Furthermore, the hydrophilic pores allow for liquid connectivity between the water in the catalyst layer and that throughout the DM to the channel. This results in a more linear response in the catalyst-layer capillary pressure, meaning that while one loses the smoothing function of pressure fluctuations provided by the MPL, one gains a lower capillary pressure for each boundary condition. In other words, the saturation in the catalyst layer is lower. These various MPL tradeoffs need to be studied in more depth both experimentally and in full-cell simulations to verify their validity and impact. Of course, if there is minimal water in the system, no case shows, nor should one expect, that an MPL increases performance based on better mass-transfer effects. The above

plausible MPL impact (i.e., point source instead of uniform face source) underscores the need to measure the capillary pressure – saturation relationship using typical cell operating conditions and components.

A couple of final points should be made. First, the above simulations utilize the values of the equilibrium capillary pressure – saturation relationship that are fit for an entire DM. It is then assumed that in the steady-state simulation, the relationships remain valid and thus are independent of thickness. While this should be more-or-less true for a uniform medium, typically GDLs are not necessarily uniform in either structure or hydrophobic content. For example, we have seen possible surface densification through x-ray tomography studies (not shown), and Los Alamos National Laboratory has shown a Teflon distribution as well [97]. Neutron imaging has also shown complex water profiles in the GDL [42, 50], which are probably due to nonuniform properties and PCI flow effects as discussed in the introduction. It is unknown how much error the above assumption causes. The capillary pressure – saturation relationships need to be validated do understand the impacts of thickness, boundary conditions, temperature gradients, etc.

Conclusions

A two-phase model developed was updated to include the use of experimentally measured capillary pressure – saturation relationships. This was accomplished through the introduction of a Gaussian contact-angle distribution into the property equations. This change allows for a better macroscopic description of multiphase flow in the diffusion media as well as better computational convergence. The updated model was used to simulate various limiting-case scenarios of water and gas transport in fuel-cell diffusion media. Analysis of these results

demonstrates that liquid convection through the diffusion medium does not cause a significant increase in saturation to appreciably affect gas-phase diffusion. Instead, interfacial or boundary conditions can result in significant mass-transfer resistance caused by the higher capillary pressures at the boundaries and the steepness of the capillary pressure – saturation relationship. The model was also used to examine the impact of microporous layers, showing that they dominate the response of the overall diffusion medium, with their primary mass-transfer-related effect seeming to be one of limiting the water injection sites into the more porous gas-diffusion layer. Overall, the key attributes to characterizing fuel-cell diffusion media are the capillary pressure – saturation and the tortuosity (i.e., effective diffusion coefficient) – saturation relationships.

Acknowledgements

The author would like to acknowledge helpful discussions and data from Drs. Jeffrey Gostick, Rodney Borup, and Rangachary Mukundan, Mr. Perry Cheung, and Ms. Haluna Gunterman. This work was supported by the Assistant Secretary for Energy Efficiency and Renewable Energy, Office of Hydrogen, Fuel Cell, and Infrastructure Technologies, of the U. S. Department of Energy under contract number DE-AC02-05CH11231.

List of Symbols

c_T = total concentration, mol cm^{-3}

$D_{i,j}$ = binary diffusion coefficient between species *i* and *j*, $cm^2\ s^{-1}$

D_{K_i} = Knudsen diffusion coefficient of species *i*, $cm^{2\ -1}$

f_{HI} = fraction of hydrophilic pores

$f_{r,k}$ = fraction of the PSD made up of distribution *k*

$f_{\theta,n}$ = fraction of the CAD made up of distribution *n*

F = Faraday's constant, 96487 C $equiv^{-1}$

i = superficial current density, A cm^{-2}

k_k = effective permeability of phase *k*, cm^2

k_r = relative permeability, cm^2

k_{sat} = absolute permeability or permeability at complete saturation, cm^2

k_T = thermal conductivity, W $cm^{-1}\ K^{-1}$

l_m = thickness of layer *m*, cm

M_i = molar mass of species *i*, g mol^{-1}

$\mathbf{N}_i$ = superficial flux density of species *i*, mol $cm^{-2}\ s^{-1}$

p^{vap} = vapor pressure of water, bar

p_C = capillary pressure, bar

p_i = partial pressure of species *i*, bar

p_L = hydraulic or liquid pressure, bar

p_k = total pressure of phase *k*, bar

q = heat flux, W cm^{-2}

r = pore radius, μm

r_c = critical pore radius, μm

$\bar{r}$ = average (mean) pore radius, μm

$\bar{r}_K$ = average Knudsen radius, μm

$r_{o,k}$ = characteristic radius of distribution k, μm

R = universal gas constant, 8.3143 J mol^{-1} K^{-1}

s_k = characteristic spread of distribution k

S = saturation, volume of pores filled with liquid

S^* = saturation calculated using equation 17

S_e = effective saturation, as calculated by Eq. 25

S_r = residual saturation

T = absolute temperature, K

v_k = velocity of phase k, cm/s

$\overline{V_i}$ = (partial) molar volume of species i, cm^3 mol^{-1}

$V(r)$ = normalized volume of pores or radius r, μm^{-1}

x_i = mole fraction of species i

Y = general property per unit volume of the medium

Greek

ε_i = porosity or volume fraction of phase i

Φ = potential, V

γ = surface tension, N cm^{-1}

μ_k = viscosity of phase *k*, bar s

θ = contact angle, degrees

$\theta_{o,n}$ = characteristic contact angle of distribution *n*, degrees

ρ_i = density of phase *i*, g cm^{-3}

σ = electronic conductivity, S cm^{-1}

σ_n = deviation of distribution *n*, degrees

τ_G = tortuosity of the gas phase

$\Psi(\theta)$= contact-angle distribution

Subscripts

0 = bulk or standard value

G = gas phase

GDL= gas-diffusion layer

L = liquid phase

MPL= microporous layer

w = water

References

[1] A.Z. Weber, R. Balliet, H.P. Gunterman, J. Newman, in: M. Schlesinger (Ed.), Modern Aspects of Electrochemistry, vol. 43, Springer, New York, 2009, p. 273.

[2] A.Z. Weber, J. Newman, Chemical Reviews, 104 (2004) 4679.

[3] C.Y. Wang, Chemical Reviews, 104 (2004) 4727.

[4] N. Djilali, Energy, 32 (2007) 269.

[5] J.H. Nam, M. Kaviany, Int. J. Heat Mass Transfer, 46 (2003) 4595.

[6] M.C. Leverett, Petroleum Division Transactions of the American Institute of Mining and Metallurgical Engineers, 142 (1941) 152.

[7] E.C. Kumbur, K.V. Sharp, M.M. Mench, J. Power Sources, 168 (2007) 356.

[8] E.C. Kumbur, K.V. Sharp, M.M. Mench, J. Electrochem. Soc., 154 (2007) B1315.

[9] T. Berning, M. Odgaard, S.K. Kaer, Journal of the Electrochemical Society, 156 (2009) B1301.

[10] A.T. Corey, Producer's Monthly, 18 (1954) 38.

[11] R.H. Brooks, A.T. Corey, Hydraulic properties of porous media, Hydrology Papers, Fort Collins, Colorado, Colorado State University, 1964.

[12] M.T. Vangenuchten, Soil Science Society of America Journal, 44 (1980) 892.

[13] R.E. De La Rue, C.W. Tobias, J. Electrochem. Soc., 106 (1959) 827.

[14] M.J. Martinez, S. Shimpalee, J.W. Van Zee, J. Electrochem. Soc., 156 (2009) B80.

[15] D.A.G. Bruggeman, Annalen Der Physik, 24 (1935) 636.

[16] P.K. Sinha, P.P. Mukherjee, C.Y. Wang, Journal of Materials Chemistry, 17 (2007) 3089.

[17] P.K. Sinha, C.Y. Wang, Electrochim. Acta, 52 (2007) 7936.

[18] K.J. Lee, J.H. Nam, C.J. Kim, Electrochim. Acta, 54 (2009) 1166.

[19] J.T. Gostick, M.A. Ioannidis, M.W. Fowler, M.D. Pritzker, J. Power Sources, 173 (2007) 277.

[20] B. Markicevic, A. Bazylak, N. Djilali, J. Power Sources, 171 (2007) 706.

[21] M. Rebai, M. Prat, J. Power Sources, 192 (2009) 534.

[22] B. Markicevic, N. Djilali, Physics of Fluids, 18 (2006).

[23] M.M. Tomadakis, S.V. Sotirchos, AIChE J., 39 (1993) 397.

[24] M.M. Mezedur, M. Kaviany, W. Moore, AIChE J., 48 (2002) 15.

[25] D. Wood, J. Davey, P. Atanassov, R. Borup, ECS Transactions, 3 (1) (2006) 753.

[26] M.J. Martinez, S. Shimpalee, J.W. Van Zee, A.V. Sakars, J. Electrochem. Soc., 156 (2009) B558.

[27] T.V. Nguyen, G. Lin, H. Ohn, X. Wang, Electrochemical and Solid State Letters, 11 (2008) B127.

[28] P. Cheung, J.D. Fairweather, D.T. Schwartz, J. Power Sources, 187 (2009) 487.

[29] J.D. Fairweather, P. Cheung, J. St-Pierre, D.T. Schwartz, Electrochemistry Communications, 9 (2007) 2340.

[30] K.G. Gallagher, R.M. Darling, T.W. Patterson, M.L. Perry, J. Electrochem. Soc., 155 (2008) B1225.

[31] J.T. Gostick, M.W. Fowler, M.A. Ioannidis, M.D. Pritzker, Y.M. Volfkovich, A. Sakars, J. Power Sources, 156 (2006) 375.

[32] J.T. Gostick, M.A. Ioannidis, M.W. Fowler, M.D. Pritzker, Electrochemistry Communications, 10 (2008) 1520.

[33] V. Gurau, M.J. Bluemle, E.S. De Castro, Y.M. Tsou, J.A. Mann, T.A. Zawodzinski, J. Power Sources, 160 (2006) 1156.

[34] E.C. Kumbur, K.V. Sharp, M.M. Mench, J. Electrochem. Soc., 154 (2007) B1295.

[35] J. Benziger, J. Nehlsen, D. Blackwell, T. Brennan, J. Itescu, J. Membr. Sci., 261 (2005) 98.

[36] D. Gerteisen, T. Heilmann, C. Ziegler, J. Power Sources, 187 (2009) 165.

[37] K.S. Chen, M.A. Hickner, D.R. Noble, International Journal of Energy Research, 29 (2005) 1113.

[38] J.T. Gostick, M.A. Ioannidis, M.W. Fowler, M.D. Pritzker, in: U. Pasaogullari, C.Y. Wang (Eds.), Modern Aspects of Electrochemistry, vol. 45, Springer, New York, 2009.

[39] R. Fluckiger, S.A. Freunberger, D. Kramer, A. Wokaun, G.G. Scherer, F.N. Buchi, Electrochim. Acta, 54 (2008) 551.

[40] D.R. Baker, D.A. Caulk, K.C. Neyerlin, M.W. Murphy, J. Electrochem. Soc., 156 (2009) B991.

[41] C. Ziegler, D. Gerteisen, J. Power Sources, 188 (2009) 184.

[42] M.A. Hickner, N.P. Siegel, K.S. Chen, D.S. Hussey, D.L. Jacobson, M. Arif, J. Electrochem. Soc., 155 (2008) B427.

[43] A. Turhan, K. Heller, J.S. Brenizer, M.M. Mench, J. Power Sources, 160 (2006) 1195.

[44] J.J. Kowal, A. Turhan, K. Heller, J. Brenizer, M.M. Mench, J. Electrochem. Soc., 153 (2006) A1971.

[45] R. Mukundan, J.R. Davey, T. Rockward, J.S. Spendelow, B.S. Pivovar, D.S. Hussey, D.L. Jacobson, M. Arif, R.L. Borup, ECS Transactions, 11 (1) (2007) 411.

[46] I. Manke, C. Hartnig, N. Kardjilov, M. Messerschmidt, A. Hilger, M. Strobl, W. Lehnert, J. Banhart, Appl. Phys. Lett., 92 (2008).

[47] I. Manke, C. Hartnig, M. Grunerbel, W. Lehnert, N. Kardjilov, A. Haibel, A. Hilger, J. Banhart, H. Riesemeier, Appl. Phys. Lett., 90 (2007) 3.

[48] S. Litster, D. Sinton, N. Djilali, J. Power Sources, 154 (2006) 95.

[49] P.K. Sinha, P. Halleck, C.Y. Wang, Electrochemical and Solid State Letters, 9 (2006) A344.

[50] A.Z. Weber, M.A. Hickner, Electrochim. Acta, 53 (2008) 7668.

[51] S. Kim, M.M. Mench, J. Membr. Sci., 328 (2009) 113.

[52] A.Z. Weber, J. Newman, J. Electrochem. Soc., 153 (2006) A2205.

[53] E. Birgersson, M. Noponen, M. Vynnycky, J. Electrochem. Soc., 152 (2005) A1021.

[54] J. Ramousse, J. Deseure, O. Lottin, S. Didierjean, D. Maillet, J. Power Sources, 145 (2005) 416.

[55] Y.Y. Shan, S.Y. Choe, J. Power Sources, 145 (2005) 30.

[56] H. Ju, H. Meng, C.Y. Wang, Int. J. Heat Mass Transfer, 48 (2005) 1303.

[57] G.L. Hu, J.R. Fan, Energy Fuels, 20 (2006) 738.

[58] H.C. Ju, C.Y. Wang, S. Cleghorn, U. Beuscher, J. Electrochem. Soc., 153 (2006) A249.

[59] Y. Wang, C.Y. Wang, J. Electrochem. Soc., 153 (2006) A1193.

[60] R.J. Balliet, K.E. Thomas-Alyea, J. Newman, ECS Transactions, 16(2) (2008) 285.

[61] S. Kim, B.K. Ahn, M.M. Mench, J. Power Sources, 179 (2008) 140.

[62] M. Oszcipok, A. Hakenjos, D. Riemann, C. Hebling, Fuel Cells, 7 (2007) 135.

[63] A.Z. Weber, R.M. Darling, J. Newman, J. Electrochem. Soc., 151 (2004) A1715.

[64] T.E. Springer, T.A. Zawodzinski, M.S. Wilson, S. Gottesfeld, J. Electrochem. Soc., 143 (1996) 587.

[65] F.A.L. Dullien, Porous Media: Fluid Transport and Pore Structure, Academic Press, Inc., New York, 1992.

[66] J. Bear, Dynamics of Fluids in Porous Media, Dover Publications, Inc., New York, 1988.

[67] J. Ramousse, S. Didierjean, O. Lottin, D. Maillet, International Journal of Thermal Sciences, 47 (2008) 1.

[68] M. Khandelwal, M.M. Mench, J. Power Sources, 161 (2006) 1106.

[69] J.T. Gostick, M.W. Fowler, M.D. Pritzker, M.A. Ioannidis, L.M. Behra, J. Power Sources, 162 (2006) 228.

[70] J.P. Feser, A.K. Prasad, S.G. Advani, J. Power Sources, 162 (2006) 1226.

[71] J. Ihonen, F. Jaouen, G. Lindbergh, A. Lundblad, G. Sundholm, J. Electrochem. Soc., 149 (2002) A448.

[72] V. Gurau, M.J. Bluemle, E.S. De Castro, Y.M. Tsou, T.A. Zawodzinski, J.A. Mann, J. Power Sources, 165 (2007) 793.

[73] M.V. Williams, E. Begg, L. Bonville, H.R. Kunz, J.M. Fenton, J. Electrochem. Soc., 151 (2004) A1173.

[74] M. Mathias, J. Roth, J. Fleming, W. Lehnert, in: W. Vielstich, A. Lamm, H.A. Gasteiger (Eds.), Handbook of Fuel Cells: Fundamentals, Technology, and Applications, Vol. 3, John Wiley & Sons, Inc., New York, 2003.

[75] Toray, GDL specification sheet, model number TGP-H-090.

[76] SGLCarbon, GDL specification sheet SGL 24 series GDLs.

[77] A.Z. Weber, J. Newman, J. Electrochem. Soc., 152 (2005) A677.

[78] U. Pasaogullari, C.Y. Wang, Electrochim. Acta, 49 (2004) 4359.

[79] D. Zwillinger (Ed.), CRC Mathematical Tables and Formulae, 31st Ed., CRC Press, Inc., Boca Raton, FL, 2003.

[80] J.T. Gostick, M.A. Ioannidis, M.W. Fowler, M.D. Pritzker, J. Power Sources (2009) in press.

[81] A.R. Kovscek, C.J. Radke, Colloids and Surfaces a-Physicochemical and Engineering Aspects, 117 (1996) 55.

[82] A.R. Kovscek, H. Wong, C.J. Radke, AIChE J., 39 (1993) 1072.

[83] E. Kimball, T. Whitaker, Y.G. Kevrekidis, J.B. Benziger, AIChE J., 54 (2008) 1313.

[84] U. Pasaogullari, P.P. Mukherjee, C.Y. Wang, K.S. Chen, J. Electrochem. Soc., 154 (2007) B823.

[85] P.C. Sui, N. Djilali, J. Power Sources, 161 (2006) 294.

[86] A. Bazylak, D. Sinton, Z.S. Liu, N. Djilali, J. Power Sources, 163 (2007) 784.

[87] J.B. Ge, A. Higier, H.T. Liu, J. Power Sources, 159 (2006) 922.

[88] A.Z. Weber, Electrochim. Acta, 54 (2008) 311.

[89] E.C. Kumbur, K.V. Sharp, M.M. Mench, J. Power Sources, 161 (2006) 333.

[90] J.S. Newman, Electrochemical Systems, Prentice Hall, Englewood Cliffs, New Jersey, 1991.

[91] D. Gerteisen, T. Heilmann, C. Ziegler, J. Power Sources, 177 (2008) 348.

[92] K. Karan, H. Atiyeh, A. Phoenix, E. Halliop, J. Pharoah, B. Peppley, Electrochemical and Solid State Letters, 10 (2007) B34.

[93] Z.G. Qi, A. Kaufman, J. Power Sources, 109 (2002) 38.

[94] J.T. Gostick, M.A. Ioannidis, M.W. Fowler, M.D. Pritzker, Electrochemistry Communications, 11 (2009) 576.

[95] M. Adachi, T. Navessin, Z. Xie, B. Frisken, S. Holdcroft, J. Electrochem. Soc., 156 (2009) B782.

[96] S. Kim, M.M. Mench, J. Electrochem. Soc., 156 (2009) B353.

[97] R. Borup, Water Transport Exploratory Studies, DOE Hydrogen Program Annual Merit Review, Crystal City, VA, 2007.

Captions

Figure 1. (a) Differential pore-size distribution data (points) for a SGL24BC diffusion medium from reference [25] and fit (line) using equations 12 and 14 with the values in Table I; and (b) the separate MPL and GDL distributions.

Figure 2. Data (points) and model (solid) of saturation as a function of capillary pressure for SGL10AA (dark circle), SGL10BA (dark square) and Toray (light diamond) GDLs where the inset is an expanded view around a capillary pressure of zero for the Toray GDL. The data are compiled from the literature,[28, 29, 34, 80] the dotted line is that predicting using our previous approach;[63] the fit parameters are given in Table I with the SGL10BA CAD angle and deviation of 116°, 2° for filling and 57°, 5° for drainage, respectively.

Figure 3. Saturation – capillary pressure relationship showing hysteresis both from the data[38] (symbols) and the simulation (lines) for a Toray 120C GDL. The curves show the full injection (red) and drainage curves (blue) as well as drainage curves after partial injection and an injection after partial drainage (dashed line). The full drainage and injection CADs were both fit using a bimodal distribution and PSD in Table I.

Figure 4. (a) Changes in the capillary pressure – saturation relationship for different PSD and CAD widths, with the Toray PSD and a CAD normalized to zero capillary pressure. The dotted line denotes 0.25 saturation, which is the fixed point to measure the impact of the CAD (b) and PSD (c) widths on capillary pressure changes for different contact angles and pore sizes.

Figure 5. Calculated gas and liquid relative permeability as a function of saturation for the Toray and SGL GDLs from Table I; also shown for comparison is a 5th order power-law dependence for the relative permeabilities.

Figure 6. Calculated gas and liquid effective permeabilities and mean Knudsen radius for SGL (top) and Toray (bottom) GDLs.

Figure 7. Boundary conditions and governing equations used for the DM modeling. The governing transport equations are given in brackets and for liquid pressure, equation 7 is the transport equation whereas the actual liquid pressure is calculated by equation 26.

Figure 8. Simulated limiting current density as a function of total liquid flux for four cases: the base case using the SGL GDL properties in Table I; the base case with the addition of 100 μm holes; cases where the smaller- and larger-pore branches of the SGL PSD have CADs using angles of 107 or 117°, respectively, and vice versa.

Figure 9. Calculated oxygen partial pressure at the liquid-injection or left side as a function of the channel or right-side capillary-pressure boundary condition for different CADs with all other properties from Table I.

Figure 10. Calculated oxygen partial pressure at the liquid-injection side as a function of the gas-phase tortuosity parameters (see equation 28); all other properties are in Table I.

Figure 11. Calculated oxygen partial pressure (a) and capillary pressure (b) at the liquid-injection side as a function of the channel capillary-pressure boundary condition for different cases involving MPLs. The cases include a DM with a 2°C temperature

gradient, an MPL with a different GDL saturation effect, and an MPL with the saturation effect and 15% hydrophilic pores; all other properties are in Table I

Table I. Fit and literature property data for the different DM components.

Table I. Fit and literature property data for the different DM components.

Parameter		Value			
		SGL	Toray	MPL	
PSD properties					
Characteristic pore radii	$r_{o,1}$	15	15	3.0	μm
	$r_{o,2}$	23	n/a	0.07	μm
Characteristic pore widths	s_1	0.22	0.20	1.28	
	s_2	0.67	n/a	0.75	
Fraction that is distribution 1	$f_{r,1}$	0.38	1	0.98	
Residual liquid saturation		0.08	0.05	0	
Porosity [75, 76]	ε	0.8	0.7	0.3	
Thickness[75, 76]	δ	0.019	0.03	0.0045	cm
Gas-volume fraction exponent	n			1.5	
Absolute permeability[69-74]	k_{sat}	3×10^{-7}	0.8×10^{-7}	5×10^{-10}	cm^2
CAD properties					
Characteristic angle	θ_o	112 50*	93	110	°
Characteristic deviation	σ	9 6*	10	1	°
Thermal conductivity[67, 68]	k_T	0.35	1.2	0.2	$W\ m^{-1}\ K^{-1}$

*For drainage curve

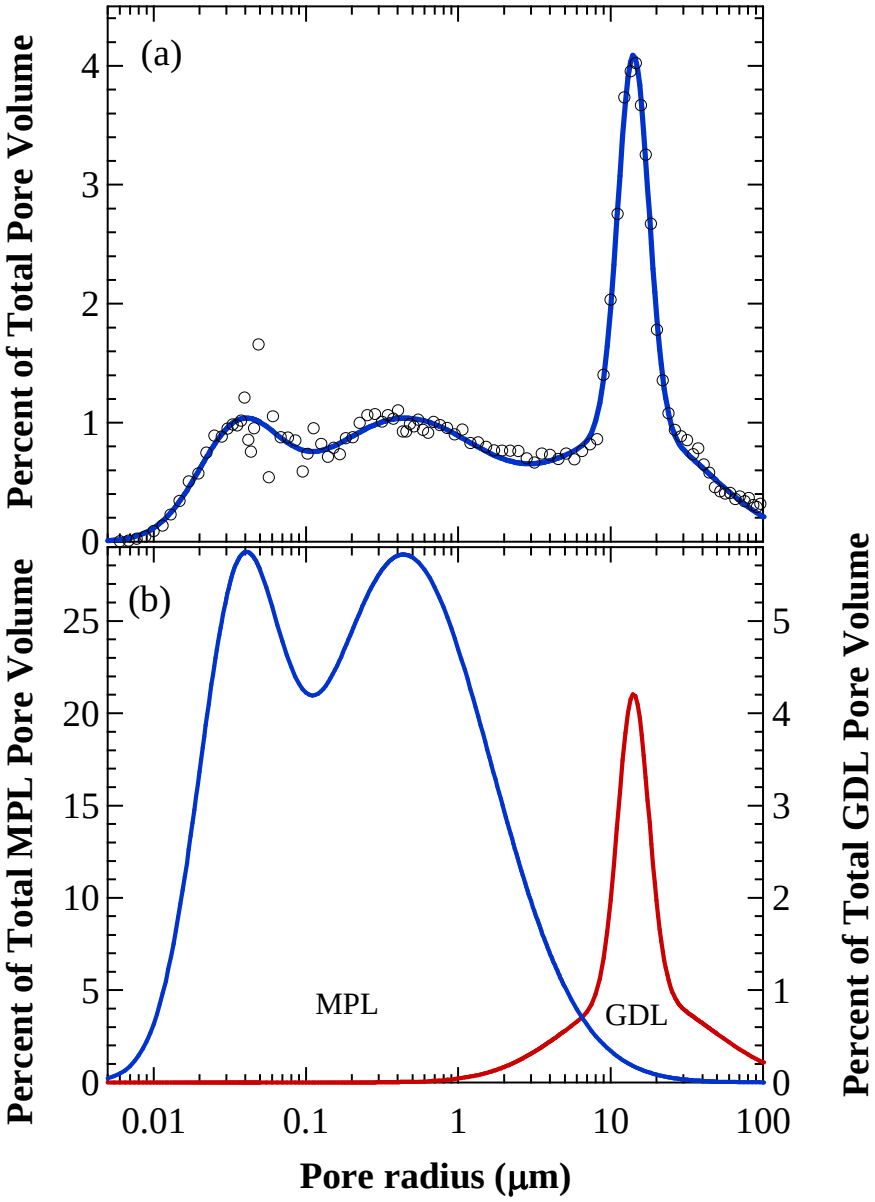

Figure 1. (a) Differential pore-size distribution data (points) for a SGL24BC diffusion medium from reference [25] and fit (line) using equations 12 and 14 with the values in Table I; and (b) the separate MPL and GDL distributions.

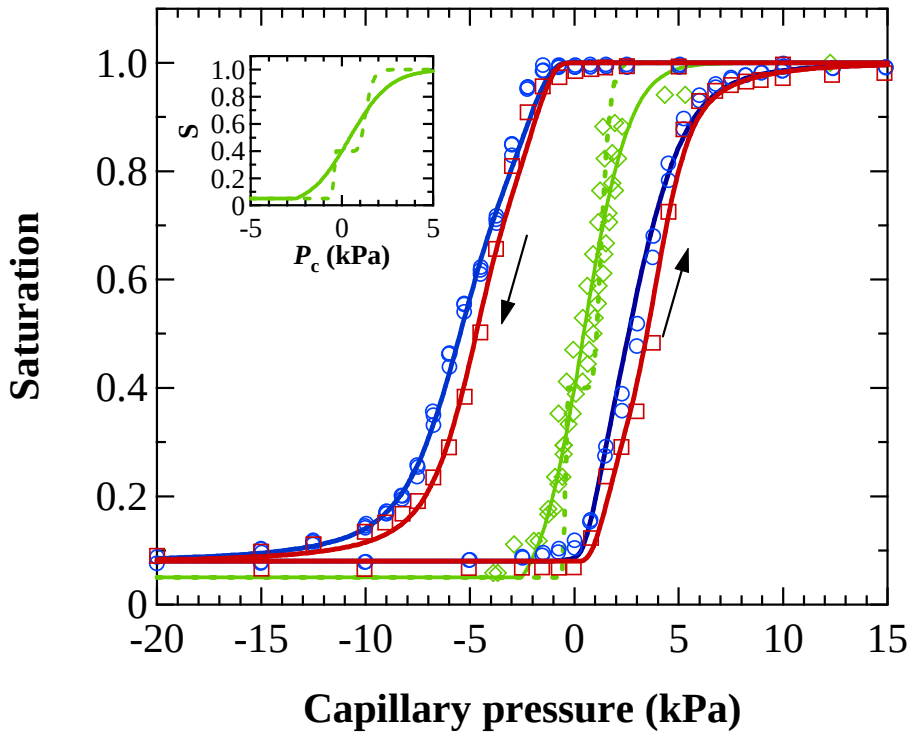

Figure 2. Data (points) and model (solid) of saturation as a function of capillary pressure for SGL10AA (dark circle), SGL10BA (dark square) and Toray (light diamond) GDLs where the inset is an expanded view around a capillary pressure of zero for the Toray GDL. The data are compiled from the literature,[28, 29, 34, 80] the dotted line is that predicting using our previous approach;[63] the fit parameters are given in Table I

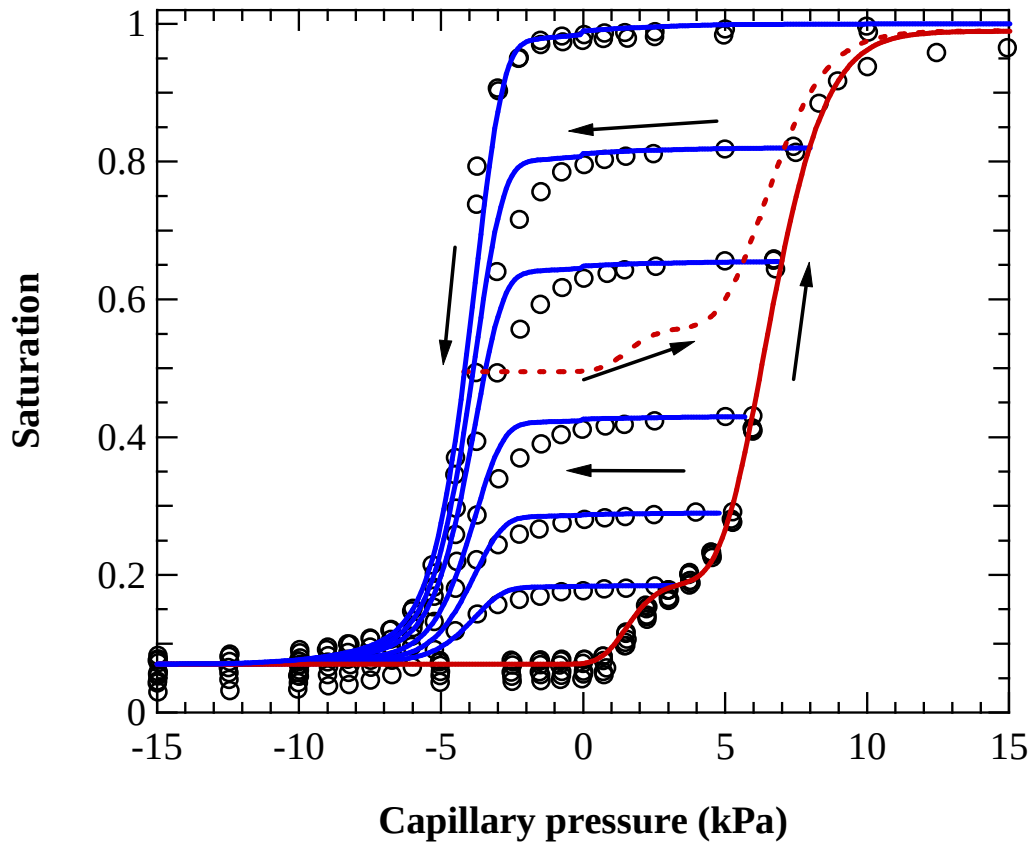

Figure 3. Saturation – capillary pressure relationship showing hysteresis both from the data[38] (symbols) and the simulation (lines) for a Toray 120C GDL. The curves show the full injection (red) and drainage curves (blue) as well as drainage curves after partial injection and an injection after partial drainage (dashed line). The full drainage and injection CADs were both fit using a bimodal distribution and PSD in Table I.

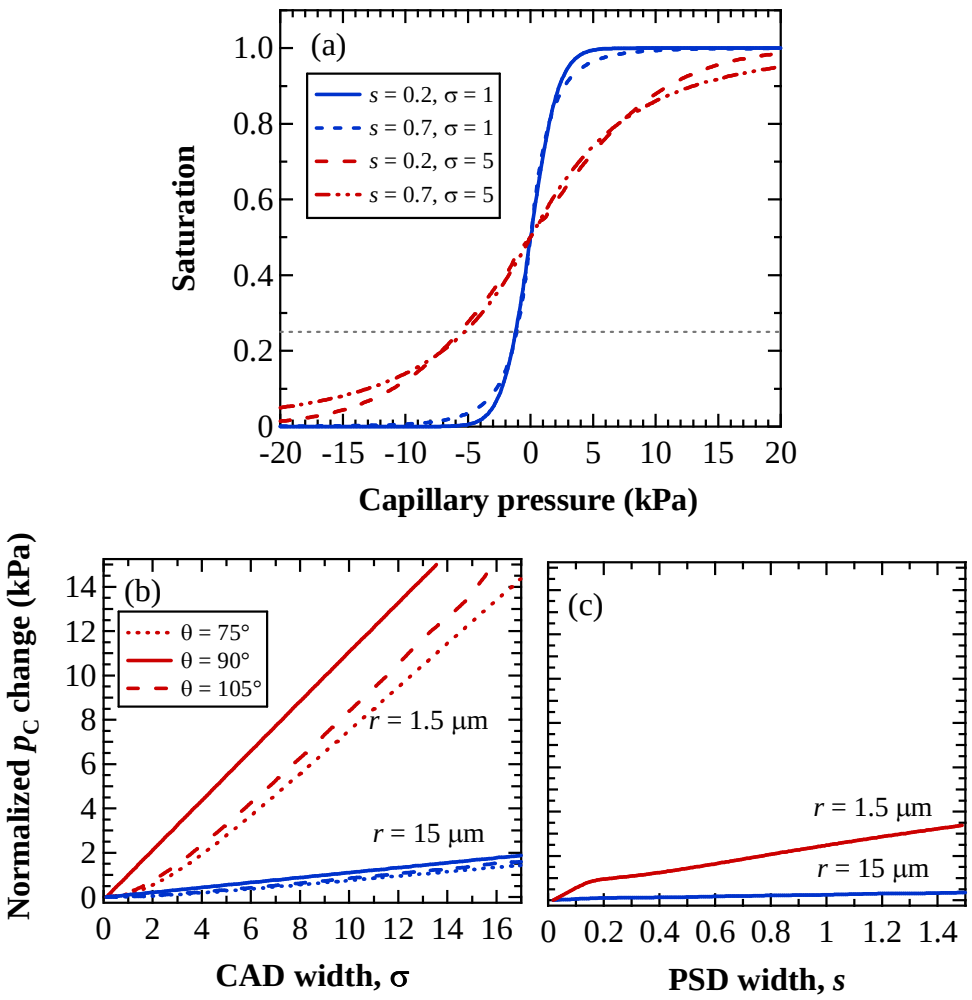

Figure 4. (a) Changes in the capillary pressure – saturation relationship for different PSD and CAD widths, with the Toray PSD and a CAD normalized to zero capillary pressure. The dotted line denotes 0.25 saturation, which is the fixed point to measure the impact of the CAD (b) and PSD (c) widths on capillary pressure changes for different contact angles and pore sizes.

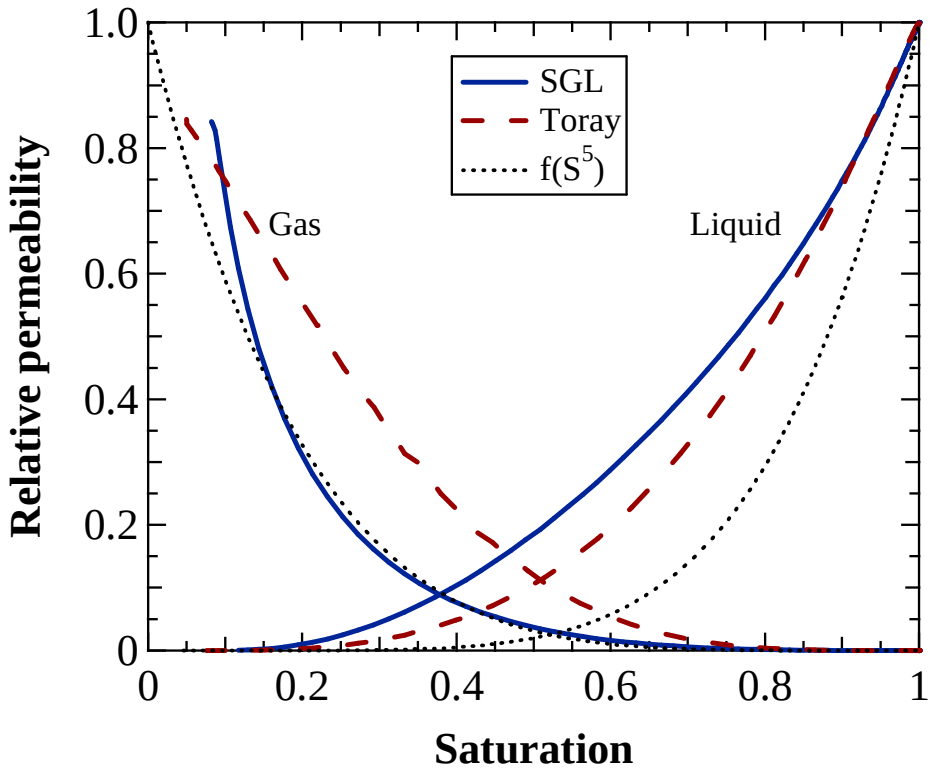

Figure 5. Calculated gas and liquid relative permeability as a function of saturation for the Toray and SGL GDLs from Table I; also shown for comparison is a 5th order power-law dependence for the relative permeabilities.

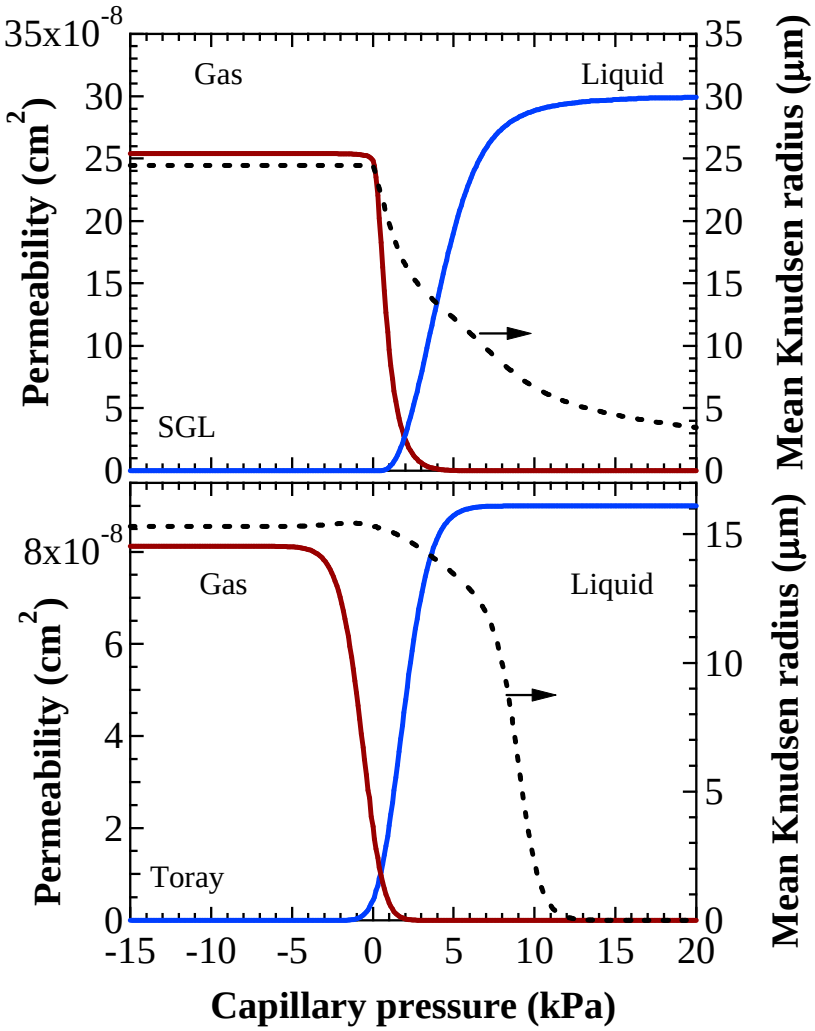

Figure 6. Calculated gas and liquid effective permeabilities and mean Knudsen radius for SGL (top) and Toray (bottom) GDLs.

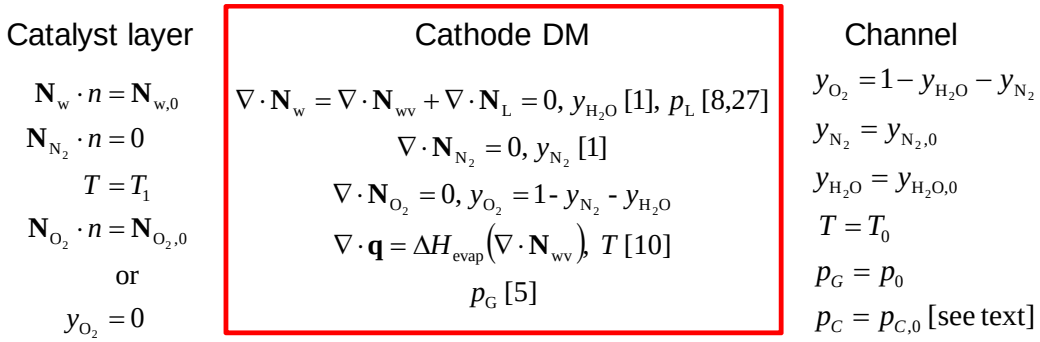

Figure 7. Boundary conditions and governing equations used for the DM modeling.

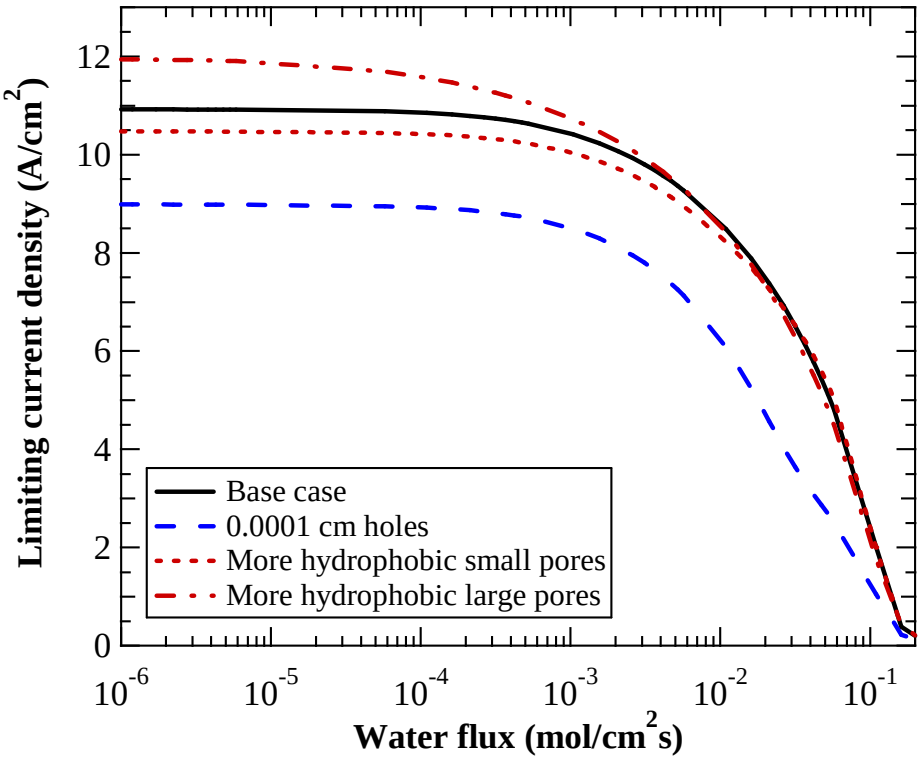

Figure 8. Simulated limiting current density as a function of total liquid flux for four cases: the base case using the SGL GDL properties in Table I; the base case with the addition of 100 μm holes; cases where the smaller- and larger-pore branches of the SGL PSD have CADs using angles of 107 or 117°, respectively, and vice versa.

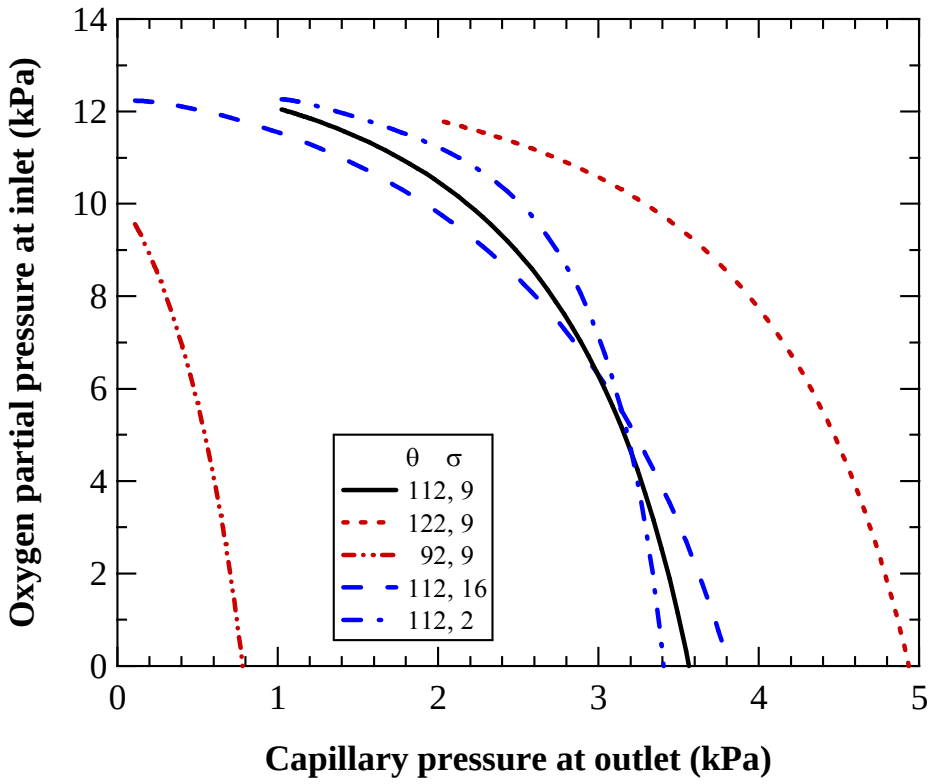

Figure 9. Calculated oxygen partial pressure at the liquid-injection or left side as a function of the channel or right-side capillary-pressure boundary condition for different CADs with all other properties from Table I.

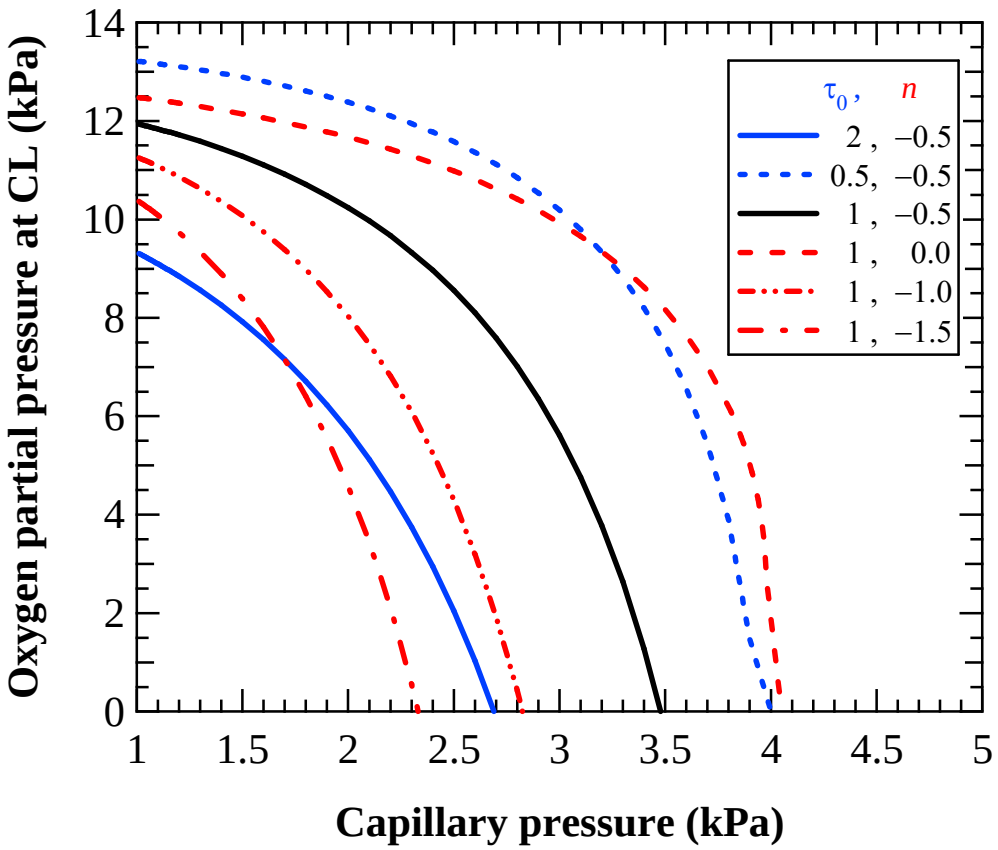

Figure 10. Calculated oxygen partial pressure at the liquid-injection side as a function of the gas-phase tortuosity parameters (see equation 28); all other properties are in Table I.

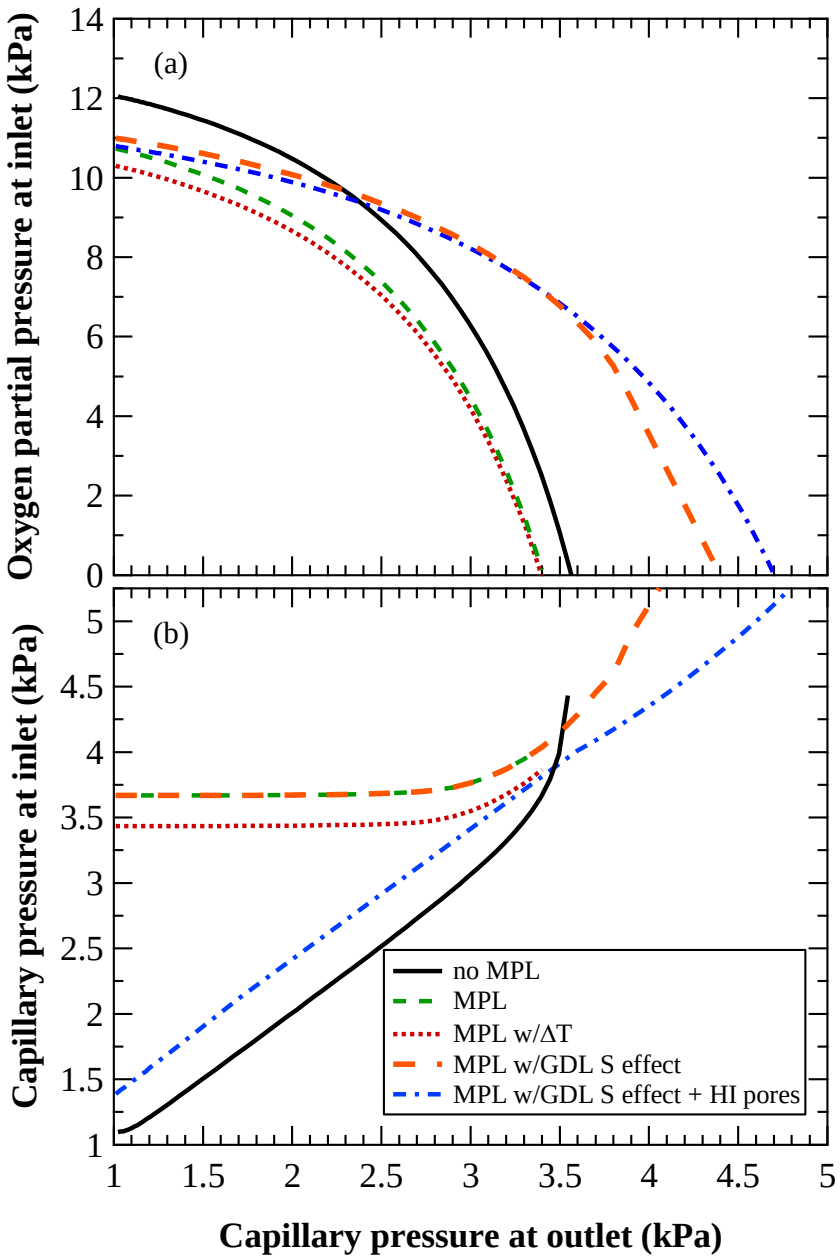

Figure 11. Calculated oxygen partial pressure (a) and capillary pressure (b) at the liquid-injection side as a function of the channel capillary-pressure boundary condition for different cases involving MPLs. The cases include a DM with a 2°C temperature gradient, an MPL with a different GDL saturation effect, and an MPL with the saturation effect and 15% hydrophilic pores; all other properties are in Table I